

Ferroelectrics

ISSN: (Print) (Online) Journal homepage: https://www.tandfonline.com/loi/gfer20

Dielectric and magnetic properties of $CuFe_2O_4$/CuO nanocomposites

Mehmet Kılıç , Naime Didem Kahya , Banu Süngü Mısırlıoğlu , Öznur Çakır & Zeynep Güven Özdemir

To cite this article: Mehmet Kılıç , Naime Didem Kahya , Banu Süngü Mısırlıoğlu , Öznur Çakır & Zeynep Güven Özdemir (2021) Dielectric and magnetic properties of $CuFe_2O_4$/CuO nanocomposites, Ferroelectrics, 571:1, 183-199

To link to this article: https://doi.org/10.1080/00150193.2020.1853752

Published online: 09 Feb 2021.

Submit your article to this journal

View related articles

View Crossmark data

Full Terms & Conditions of access and use can be found at
https://www.tandfonline.com/action/journalInformation?journalCode=gfer20

FERROELECTRICS
2021, VOL. 571, 183–199
https://doi.org/10.1080/00150193.2020.1853752

Taylor & Francis
Taylor & Francis Group

Check for updates

Dielectric and magnetic properties of $CuFe_2O_4$/CuO nanocomposites

Mehmet Kılıç[a], Naime Didem Kahya[b], Banu Süngü Mısırlıoğlu[a], Öznur Çakır[a], and Zeynep Güven Özdemir[a]

[a]Department of Physics, Yildiz Technical University, Istanbul, Turkey; [b]Faculty of Sciences, Department of Chemistry, Ankara University, Ankara, Turkey

ABSTRACT

Copper ferrite/copper oxide ($CuFe_2O_4$/CuO) nanocomposites contents were prepared by using co-precipitation and sol-gel methods. The alternating current impedance and permittivity parameters of the samples were obtained by an impedance analyzer between 10 Hz and 40 MHz. The temperature dependences of magnetization were measured in zero-field-cooled (ZFC) and field-cooled (FC) modes and hysteresis curves at 300 K were investigated. In this context, it has been determined that the 25% CuO doped copper ferrite nanomaterial was showed the reduced dielectric loss and super-capacitive ability for ultra-capacitor application at high frequencies. Additionally, the samples prepared in this work were exhibited a superparamagnetic behavior.

ARTICLE HISTORY
Received 11 March 2020
Accepted 1 September 2020

KEYWORDS
Ferrites; nanocomposites; dielectric properties; impedance spectroscopy; magnetic properties

1. Introduction

Due to their unique electromagnetic behavior, ferrite nanoparticles with the general formula MFe_2O_4 (where M: Mn, Fe, Co, Ni, Cu, Zn) have received increasing attention for several potential applications such as drug delivery, hyperthermia, catalyst, sensor, biosensor, energy storage, electromagnetic interference shielding, and microwave devices [1]. Ferrites have a spinel structured in which metal ion arrangements (M^{2+}) strongly affect the magnetic, electrical, and optical properties of the material. Among them, the low cost and eco-friendly $CuFe_2O_4$ (copper ferrite) is one of the most important inverse spinel ferrite materials. The preparation method and the heat-treatment play critical roles in the stabilization of either of the two crystallographic structures of copper ferrite, which are the tetragonal and cubic spinel phases [2]. Hydrothermal, sonochemical, sol-gel, co-precipitation, and solid-state methods are generally used for the preparation of copper ferrite [1–4]. Their inverse spinel structure and magnetic properties have been studied by Anandan et al. [5]. The results of their Mossbauer spectroscopy studies show that Fe is located both in the tetrahedral and octahedral sites in the ratio 40:60 and that $CuFe_2O_4$ nanoparticles show ferromagnetic behavior.

Furthermore, in recent years, the development of processing capabilities has led researchers to prepare composites by introducing various nanoparticles of CeO_2 [6],

CONTACT Mehmet Kılıç kilic-m@hotmail.com
© 2021 Taylor & Francis Group, LLC

ZnO [3, 7, 8], SnO_2 [9–13], MgO [14], MnO_2 [15], and Li [16] into the $CuFe_2O_4$ matrix. In these studies, structural, optical, dielectric, and magnetic properties of the copper ferrite-based nanocomposites have been widely investigated for their synthesizing methods, sintering temperatures, and doping concentrations of the nanoparticles. Additionally, copper ferrite-based devices have promising applications such as anodes for Li-ion batteries [17], high-performance catalytic applications [18–20], gas sensors [4, 21, 22], solid-oxide fuel-cell interconnect applications [23], and highly stable supercapacitor electrode applications [24].

As is known, CuO is a well-known p-type semiconductor with chemical stability, low cost, and high thermal emittance ability [25, 26]. These properties make CuO a suitable component for applications such as sensors [27] and optoelectronic devices [28]. On the other hand, $CuO/CuFe_2O_4$ nanocomposites with their tunable saturation magnetization, crystallite size, and optical bandgap [29] properties have attracted tremendous interest in their advanced applications such as new design batteries and inexpensive gas sensors [30, 31].

From this point of view, to reveal the frequency-dependent electrical properties of $CuO/CuFe_2O_4$ nanocomposites, the impedance spectroscopy technique was used. The composites have been synthesized by using the co-precipitation and sol-gel methods. We focused on examining the structural properties, the complex permittivity, AC impedance parameters, the AC conductivity, and the magnetic properties of the samples. The AC electrical parameters of the samples are given in different AC representations and discussed. In addition to the frequency dependencies of the real and imaginary parts of the complex permittivity, the conductivity as a function of the angular frequency of the samples is also discussed. Moreover, Nyquist plot analyses have been performed to determine the equivalent circuit parameters of the samples. Furthermore, we studied temperature- and field dependence of the magnetization in the temperature range and examine the blocking properties of the nanocomposites.

2. Materials and methods

2.1. Materials

$FeCl_3$, $CuCl_2$, and glacial acetic acid were purchased from Sigma-Aldrich. All chemicals were of analytical grade and used as-received for the experiments. Double distilled water was used for the preparation of the solutions.

2.2. Synthesis of $CuFe_2O_4$/CuO nanocomposites

$CuFe_2O_4$ and CuO nanoparticles were prepared by co-precipitation [15] and sol-gel methods [32], respectively. In the first step, a 0.4 M (25 ml) solution of iron chloride and 0.2 M (25 ml) solution of copper chloride were mixed in doubly distilled water. Distilled water was used as a solvent to avoid the formation of impurities in the final solutions. After this step, the 3 M (25 ml) solution of sodium hydroxide was slowly added to the salt solution dropwise. The pH of the solution was constantly monitored under magnetic stirring until a pH level of 11–12 was reached. Then, the liquid precipitate was brought to a reaction temperature of 80 °C and stirred for 1 h. The product

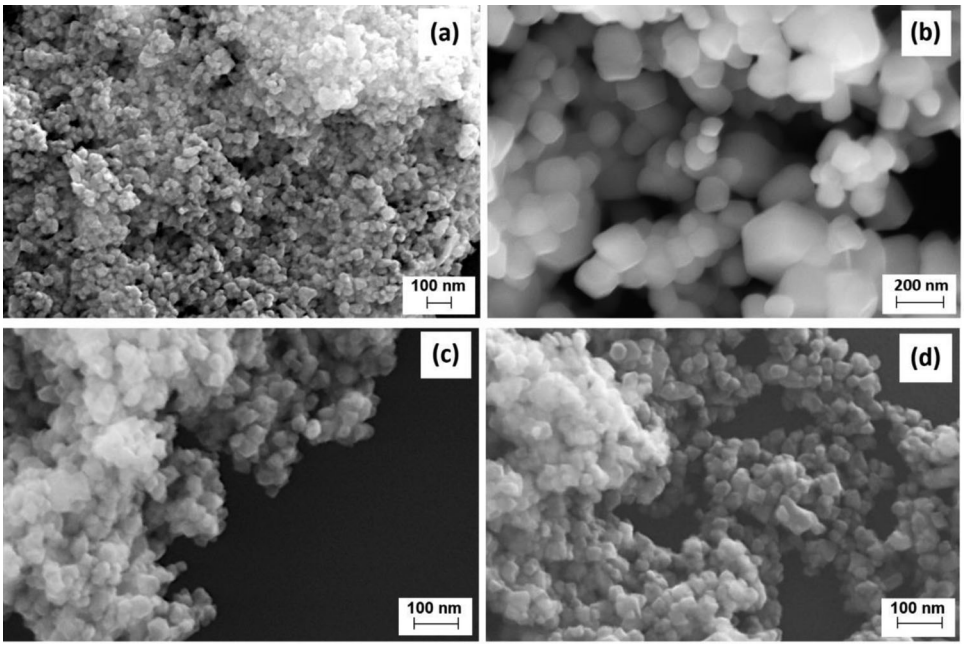

Figure 1. SEM images of (a) $CuFe_2O_4$, (b) CuO, (c) $CuFe_2O_4$/10% CuO composite and (d) $CuFe_2O_4$/25% CuO composite.

was subsequently cooled to room temperature. The precipitate was washed 3–4 times with distilled water in order to remove sodium and chloride-compound impurities. The obtained product was centrifuged for 10 min at 3000 rpm to isolate the precipitate from the solution. The precipitate was then dried overnight at 100 °C. The $CuFe_2O_4$ sample was then ground into a powder and annealed at 600 °C for 5 h.

In the second step, 0.2 M (25 ml) solution of copper chloride was prepared with distilled water in a round bottom flask. 1 ml of aqueous solution of glacial acetic acid was added to this solution and the solution was warmed to 100 °C with constant stirring. Then, 8 M of NaOH was added until the pH reached 7. The color of the solution turned from green to black, and a large amount of black precipitate formed immediately. The black precipitate was filtered out from the solution and washed 3–4 times with double distilled water. The obtained precipitate was dried in air for 24 h. The CuO sample was then ground into a powder and then annealed at 600 °C for 5 h. Finally, $CuFe_2O_4$ and CuO nanoparticles were mixed with different weight percentages of CuO (10% and 25%) to obtain $CuFe_2O_4$/CuO nanocomposites. The mixtures were heat-treated at 600 °C for 5 h.

3. Results and discussion

3.1. Scanning electron microscope (SEM) measurements

The surface morphologies of the samples were determined by using a Zeiss Supra 40VP model and SEM. Figure 1 shows the SEM images of the $CuFe_2O_4$, CuO, and the $CuFe_2O_4$/CuO composites. As shown in Fig. 1(a,b), the pure copper ferrite and pure

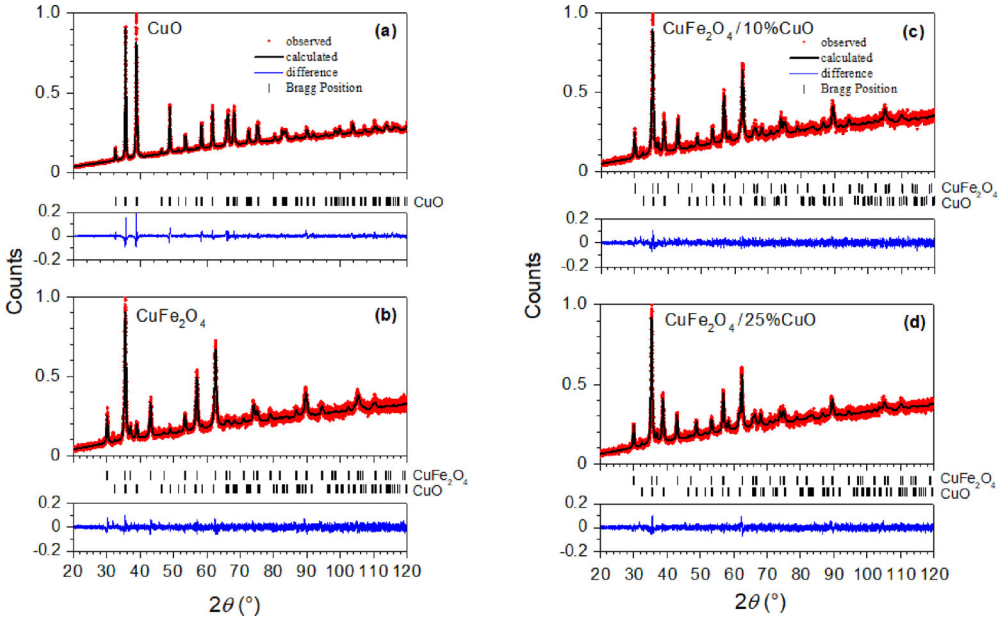

Figure 2. The XRD patterns of (a) CuO, (b) $CuFe_2O_4$, (c) $CuFe_2O_4$/10% CuO, (d) $CuFe_2O_4$/25% CuO.

copper oxide nanoparticles have both facetted structures. The average particle sizes of the $CuFe_2O_4$ and CuO were observed between 30–40 nm and 50–85 nm, respectively. The nanocomposites were observed as randomly distributed copper ferrite and copper oxide nanoparticles.

3.2 X-ray diffraction (XRD) analysis

XRD measurements were carried out using Cu-Kα radiation on a Panalytical X'PertPro diffractometer. The results are shown in Fig. 2.

Due to the use of a Cu source, a certain amount of fluorescence occurs. However, this does not impede the refinement of the spectra. Le Bail fitting was performed using JANA2006 software [33]. The space group C2/c accounts well for monoclinic CuO giving the lattice parameters $a = 4.684\,\text{A}^\circ$, $b = 3.424\,\text{A}^\circ$, and $c = 5.129\,\text{A}^\circ$ and cell angles $\alpha = 90^\circ$, $\beta = 99.4^\circ$, and $\gamma = 90^\circ$. The structure of cubic $CuFe_2O_4$ complies with the Fd-3m space group, and the analysis yields a lattice constant of $a = 8.414\,\text{A}^\circ$. As shown in Fig. 2(c,d), the XRD patterns of the composites confirm the formation of both phases ($CuFe_2O_4$ and CuO), which are coexistent in the composites. The lattice parameter of the cubic $CuFe_2O_4$ phase was found as $a = 8.410\,\text{A}^\circ$ and $a = 8.404\,\text{A}^\circ$ for the $CuFe_2O_4$/10% CuO and $CuFe_2O_4$/25% CuO composites, respectively. While the lattice parameters and the cell angles of the monoclinic CuO phase in $CuFe_2O_4$/10%CuO composite was found as $a = 4.686\,\text{A}^\circ$, $b = 3.425\,\text{A}^\circ$, $c = 5.123\,\text{A}^\circ$; $\alpha = 90^\circ$, $\beta = 99.57^\circ$, $\gamma = 90^\circ$, the $CuFe_2O_4$/25%CuO composite has the CuO phase with the lattice parameters of $a = 4.687\,\text{A}^\circ$, $b = 3.426\,\text{A}^\circ$, $c = 5.119\,\text{A}^\circ$ and the cell angles of $\alpha = 90^\circ$, $\beta = 99.48^\circ$, $\gamma = 90^\circ$.

To determine the average particle size of the samples, standard Scherrer analysis was also carried out by considering the instrumental resolution. For this purpose, we use the Scherrer formula:

$$D_p = \frac{K\lambda}{B\cos\theta} \tag{1}$$

where K is a constant which approximately equals 0.9 and λ is the wavelength of the X-ray used in the X-ray analysis. In Eq. (1), while B is the full width at half maximum (FWHM) corrected to the instrumental resolution, θ also represents the Bragg angle. The average particle sizes of the $CuFe_2O_4$, CuO, $CuFe_2O_4$/10% CuO, and $CuFe_2O_4$/25% CuO were determined as ~40 nm, ~57 nm, ~26 nm, ~27 nm, respectively. The average particle sizes are also in agreement with the SEM images discussed above.

3.3. Effective complex permittivity and AC conductivity results

Dielectric measurements were performed by NOVO Control Broadband Dielectric/Impedance analyzers with Quatro Cryosystem in the frequency interval 10 Hz–40 MHz at 300 K. The dielectric measurements were carried out with the two-point probe technique. The samples were placed between two gold electrodes with surfaces fully overlapping the faces of the samples. The active electrode area is 3.14 cm^2.

The real and imaginary components of the effective complex permittivity (ε' and ε''), as well as the AC conductivity, were measured. The effective complex permittivity is described by

$$\varepsilon* = \varepsilon' - i\varepsilon'' \tag{2}$$

where $i = \sqrt{-1}$.

The variation with frequency of the real part of effective complex permittivity and the loss tangent for $CuFe_2O_4$ and $CuFe_2O_4$/CuO nanocomposites are shown in Fig. 3(a,b), respectively. The frequency dependencies of the imaginary component of the effective complex permittivity are shown in Fig. 3(c).

As shown in Fig. 3(a), the real component of the effective complex permittivity decreases with increasing frequency. We also observe that the frequency dependence of ε' is not affected by CuO. This behavior of ε' can be explained by the Maxwell-Wagner type interfacial polarization which is in good agreement with Koop's bilayer theory [34–36]. A similar interfacial polarization was observed in many ferrite structures such as NiCuZn ferrite [37], complex hexaferrite [38], etc. Additionally, Ali et al. explained the dielectric behavior of $CuFe_2O_4$/MnO_2 nanocomposites in the context of Koop's bilayer theory [15]. In Koop's model, the dielectric medium is considered as the sum of good conducting grains which are surrounded by the poorly conducting grain boundaries. In other words, the dielectric material is defined as an inhomogeneous structure which consists of conducting and non-conducting layers. In this context, grain boundaries are more active at lower frequencies, while grains are more dominant at higher frequencies. This situation can be expressed as follows: Electrons, which are likely to be the charge carriers of the material, can move to grain boundaries by a hopping mechanism at low frequencies. If the grain boundary resistance is very high for transporting electrons from a grain to a grain boundary, the electrons accumulate at the grain

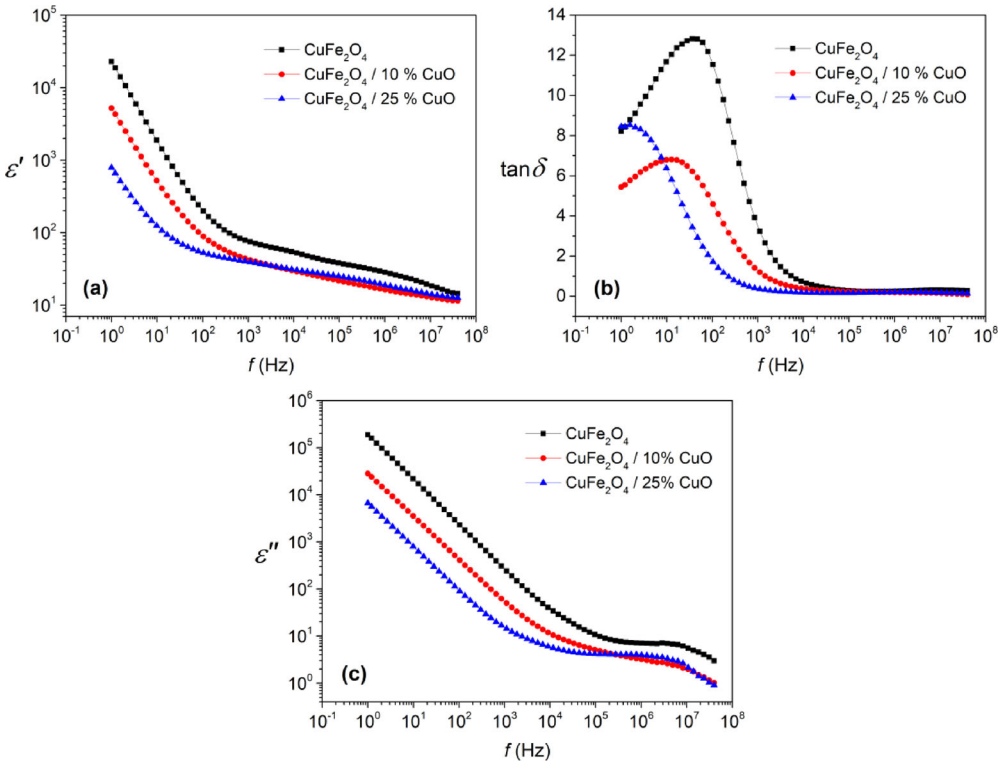

Figure 3. The frequency dependence of (a) the real part of the effective complex permittivity, (b) loss tangent, and (c) the imaginary part of the effective complex permittivity for pure $CuFe_2O_4$, $CuFe_2O_4$/10% CuO, and $CuFe_2O_4$/25% CuO composites at room temperature (300 K).

boundary resulting in a high-order polarization. The polarization, in this case, is also known as "space-charge polarization". The pile-up of electrons at the grain boundary manifests itself as an observation of high ε'-values at low frequencies. However, as the frequency of the applied electric field is increased, the probability of electrons reaching the grain boundary is reduced, and accordingly, the polarization is reduced. This state is manifested by the frequency-independent behavior of ε' at high frequencies.

In the present case, the low-frequency behavior of the real component of the effective complex permittivity of all samples is essentially due to the fact that the electronic exchange between Fe^{2+} and Fe^{3+} cations cannot follow the applied electric field. Moreover, the decrease in ε' values at low frequency with increasing CuO concentration can be attributed to the increase of the resistivity of the composites, resulting in a decrease of the numbers of mobile space-charge carriers [39]. Similar behavior of ε' has also been observed in $CuFe_2O_4$–CeO_2 and $CuFe_2O_4$–MnO_2 nanocomposites [6, 15].

The energy required for polarization in the dielectric medium is parameterized as the loss tangent, $tg\delta$. As shown in Fig. 3(b), $tg\delta$ exhibits an increase up to a certain frequency known as the dielectric relaxation frequency. It then decreases sharply, and finally, approaches zero in the high-frequency domain. Since the degree of space-charge polarization is very high at low frequencies (Fig. 3(a)), the energy required is also high. On the other hand, the polarization is highly reduced at high frequencies and $tg\delta$ decreases considerably. Moreover, we observe that 10% CuO contribution reduces the

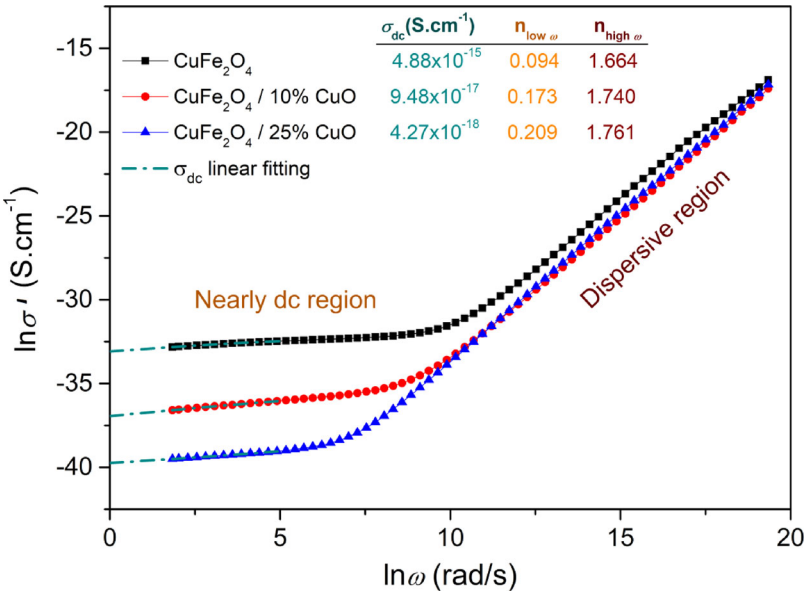

Figure 4. ln σ_{ac} versus ln ω curves for pure $CuFe_2O_4$, $CuFe_2O_4$/10% CuO, and $CuFe_2O_4$/25% CuO nanocomposites.

energy requirement by half compared to pure Cu-ferrite. However, the 25% CuO addition does not continue to reduce the energy requirement for the space-charge polarization. Additionally, observation of such a relaxation peak can be associated with the fact that the hopping frequency of localized charge carriers becomes approximately equal to the frequency of the external electric field and hence the resonance occurs [38]. It has also been clearly observed that the dielectric relaxation frequency shifts toward lower frequencies as the concentration of CuO increases in the composite (Fig. 3(b)). Since the dielectric loss peak is observed under the condition of

$$2\pi f_{\max}\tau = 1 \tag{3}$$

where $f_{\max}$ and τ are the relaxation frequency and time, respectively, it is possible to write a relation between relaxation time (τ) and the probability of jumping the charge carriers per unit time (P) [40]:

$$\tau = \frac{1}{2P} \tag{4}$$

As shown in Fig. 3(b), as the CuO nanoparticle concentration percentages increases, the relaxation time increases. According to Eq. (4), the increase in τ due to CuO indicates a reduced charge-carrier hopping probability leading to the decrease in conductivity. The consistency of this interpretation will be seen from the frequency dependence of the AC conductivity in Fig. 4. Finally, this kind of relaxation peak observed in dielectric loss spectra is due to the heterogeneous structure of the ferrite in which the components of the dielectric material involves different conductivities [41].

The imaginary part of effective complex permittivity can be calculated from,

$$\varepsilon'' = \varepsilon' \tan \delta \tag{5}$$

The frequency dependencies of the imaginary part of the effective complex permittivity of all samples at room temperature (Fig. 3(c)) display a decrease with decreasing frequency at low frequencies and an approach to a low-value in the high-frequency range. When all complex permittivity and tangent loss results are evaluated together, it was determined that the $CuFe_2O_4$/25% CuO composite has high ε' values varying between 9033.85 and 14.14 and low values which all are less than 0.21 for the frequency interval of $10^4 < f < 10^7$ Hz. From this respect, the composite may have a promising potential in high-frequency applications.

The complex conductivity ($\sigma*$) of the samples were also defined by Eq. (6)

$$\sigma* = \sigma' + j\sigma'' \tag{6}$$

In Eq. (6), the σ' and σ'' are the real and imaginary components of the $\sigma*$. The real component of the complex conductivity is the AC conductivity and is calculated as

$$\sigma' = \varepsilon_0 \omega \varepsilon'' = \sigma_{dc} + A\omega^n \tag{7}$$

where ε_0 and ω are the permittivity of free space and angular frequency, respectively. The real part of the complex conductivity can be divided into frequency-independent (σ_{dc}) and the dispersive ($A\omega^n$) parts. While the dc-conductivity arises from unrestricted random hopping of the ions, the second term is the frequency-dependent conductivity in terms of Jonscher's power law (JPL) and arises due to restricted ion hopping [42]. In Eq. (7), A is a constant defining the strength of the polarization and n is the frequency exponent signifying the charge transport mechanism of the system. The frequency exponent takes values between zero and one. Additionally, the $n = 0$ and $n = 1$ cases indicate pure resistive and pure capacitive behaviors of the material, respectively [43].

The room temperature σ' of the samples is plotted against the angular frequency, ω on a logarithmic scale and given in Fig. 4. Here, the angular frequency dependence of σ' has two different conductivity regimes: the nearly dc-conductivity (σ_{dc}) at low frequencies which is represented by a frequency-independent plateau and a dispersive region in the high-frequency domain. We observe that the AC conductivity increases with the increasing frequency and obeys the power law $A\omega^n$. Additionally, the hopping of the electrons between Fe^{2+} and Fe^{3+} ions is expected to be responsible for AC conductivity.

On the other hand, we observe in Fig. 4 that increasing the CuO concentration considerably decreases the conductivity at low frequencies. This effect can be explained by the fact that Cu^{2+} cations occupy the Fe^{3+} lattice sites thus decreasing the possibility of electron hopping between Fe^{2+} and Fe^{3+} sites.

σ_{dc} and n-values for the low and high-frequency regions for each sample are given in Fig. 4. While σ_{dc} values are determined by extrapolating the dc plateaus, n-values are calculated from the slopes of the curves described by the function $\ln \sigma_{ac} = f(\ln \omega)$ in the dispersive region.

According to the n-values which are in the range 0.048–0.085 depending on the CuO concentration, nearly dc-conductivity is the dominant mechanism in the low-frequency region. However, since the high-frequency n-values vary between 0.76 and 0.88, the AC

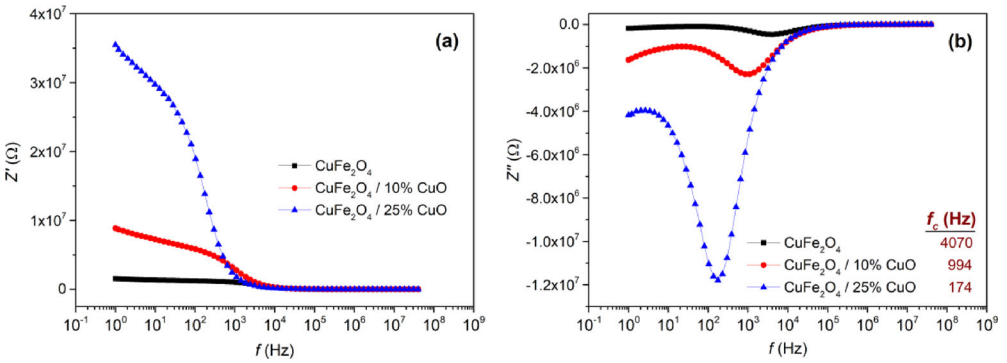

Figure 5. The frequency dependence of (a) the real and (b) imaginary components of the complex impedance function for pure $CuFe_2O_4$, $CuFe_2O_4$/10% CuO, and $CuFe_2O_4$/25% CuO composites at room temperature.

conductivity in the dispersive region can also be explained by JPL. According to the frequency exponent values, the AC conductivity can be associated with the hopping mechanism.

3.4. Complex impedance

The complex impedance function is defined by,

$$Z* = Z' - iZ'' \tag{8}$$

where $Z' = R$ and $Z'' = X_c$ represent the real and imaginary components of the complex impedance function, respectively. The variations of the real and imaginary components of the complex impedance function with frequency are shown in Fig. 5(a,b), respectively.

As seen in Fig. 5(a), the resistance takes high- and low values in the low- and high-frequency regions, respectively. In this respect, the frequency dependence of the real part of the complex impedance also confirms the relevance of Koop's bilayer theory for the samples. Since the grain boundary effect is more dominant at low frequencies, the resistivity in the low-frequency region should be higher, so that the conductivity is lower. The dominance of the grain effect at high frequencies is also represented by the high conductivity. Moreover, we observe that CuO addition significantly increases Z' at low frequencies. On the other hand, firstly the capacitive reactance (Z'') increases, then it passes through a maximum, and finally decreases with increasing frequency (cf. Fig. 5(b)). However, Z'' approaches the same value in the high-frequency domain for all samples. This behavior is another indication of the fact that there is no high-frequency polarization. Additionally, the critical frequency, f_c, at which the maximum Z'' is recorded, shifts toward lower frequencies as the amount of CuO increases. Detection of such a peak in the Z'' vs. frequency curve also indicates the presence of relaxation in the material. These peaks, recorded at relatively low frequencies, are further indications of the dominance of the grain boundary effect at low frequencies. Additionally, since the relaxation time increases as the CuO concentration increases, there is a reduced

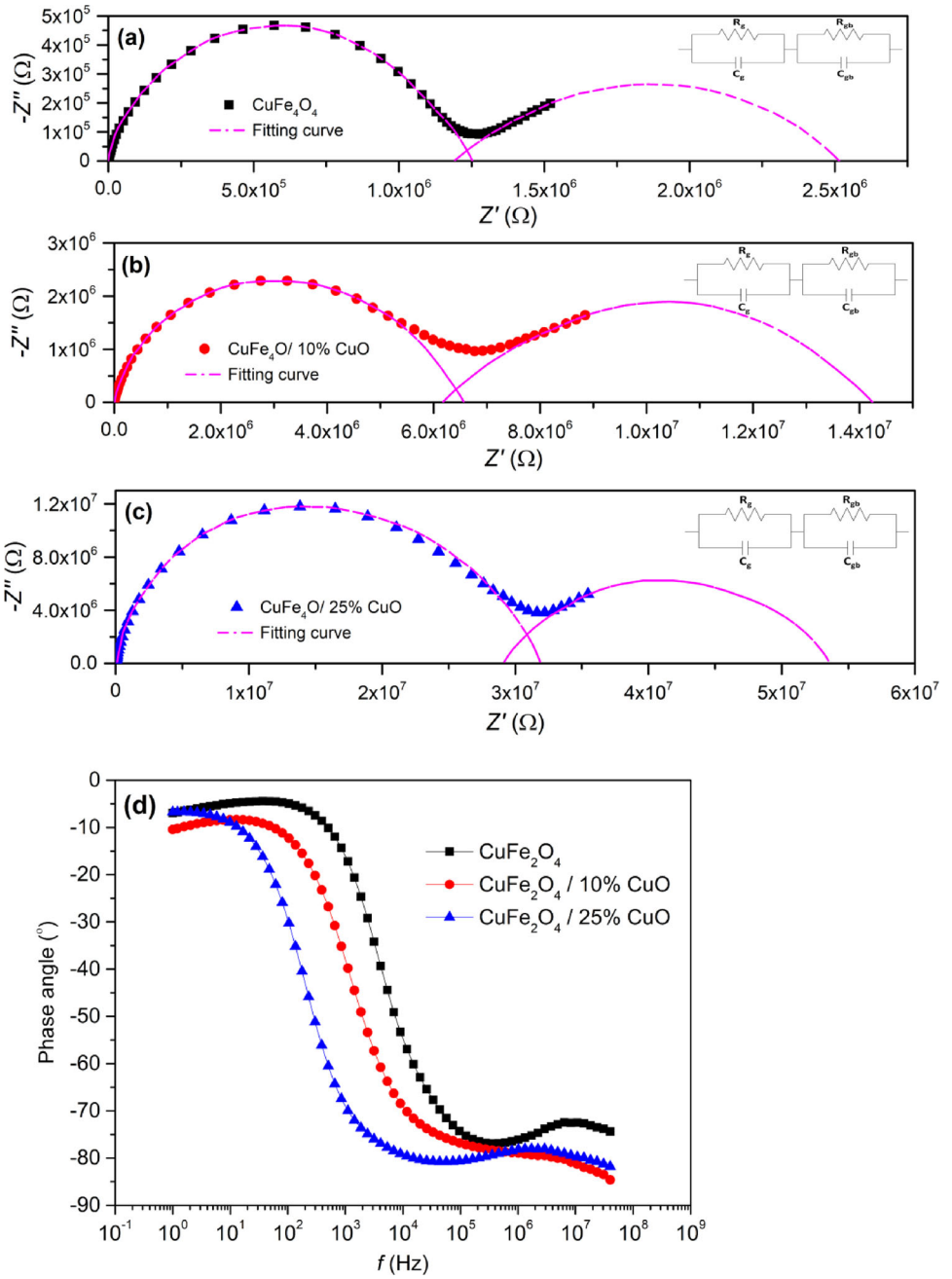

Figure 6. The Nyquist plots for (a) pure $CuFe_2O_4$, (b) $CuFe_2O_4$/10% CuO, (c) $CuFe_2O_4$/25% CuO composites, and (d) Bode plots for the samples at room temperature. The inset in the Nyquist plot is the circuit equivalent of the samples.

charge carrier hopping probability in the composites which have higher CuO content. This also manifests itself as a decrease in conductivity as shown in Fig. 4.

To determine the equivalent circuit parameters, we also consider Nyquist and Bode's plots given in Fig. 6. A series array of two parallel resistor-capacitor combinations

Table 1. Equivalent circuit parameters determined by fitting for the samples.

Sample	R_g (Ω)	R_{gb} (Ω)	C_g (F)	C_{gb} (F)
$CuFe_2O_4$	1.25×10^6	2.52×10^6	3.18×10^{-11}	6.99×10^{-12}
$CuFe_2O_4$/10% CuO	6.57×10^6	1.42×10^7	2.84×10^{-11}	4.59×10^{-12}
$CuFe_2O_4$/25% CuO	3.18×10^7	5.35×10^7	3.33×10^{-11}	9.97×10^{-12}

(R_g, C_g) and (R_{gb}, C_{gb}) were found to give good fits to the experimental data. As shown in Fig. 6(a–c), the centers of the semicircles of each sample lie below the Z'-axis implying a non-Debye type of relaxation. To determine the equivalent circuit parameters (grain resistance (R_g), grain capacitance (C_g), grain boundary resistance (R_{gb}), and grain boundary capacitance (C_{gb}), Nyquist plots were fitted. The related circuit parameters are given in Table 1.

According to Table 1, the grain boundary resistance is greater than the grain resistance for each sample. This phenomenon can be explained with the more resistive nature of the grain boundaries than grains themselves. Additionally, R_g and R_{gb} increase with increasing CuO contribution. On the other hand, grain capacitance values are in the order of 10^{-11} F, which is in good agreement with typical values of grain capacitance values [44].

The Bode plot given in Fig. 6(d) also confirms that the whole process is capacitive due to the observation of negative phase angles varying between -4.2° and -80.9°. The phase angle close to -90° was detected above 10 MHz for the 25% CuO doped Cu-ferrite. At the same frequency, the composite has also a very low dielectric loss (see Fig. 3). Reaching the phase angle of -90° has crucial importance for supercapacitor applications, since -90° represents the pure capacitive circuit element [45].

3.5. The magnetization

The temperature dependence of the magnetization $M(T)$ can provide clear evidence for the nature of magnetism in nano-sized magnetic materials. At the nanometer scale, blocking effects are expected to be found of which the characteristics depend very much on the particle size. $M(T)$ of the copper ferrite-based samples were carried out using a SQUID (Superconducting Quantum Interference Device) magnetometer in zero-field-cooled (ZFC) and field-cooled (FC) modes in 50 Oe. As shown in Fig. 7(a–c), a splitting due to spin-frustration effects is observed between ZFC and FC cases for both $CuFe_2O_4$ and its CuO-added composites. However, the ZFC and FC curves have no overlap up to the highest temperature measured. This indicates that a freezing temperature related to the onset of frustration should lie at higher temperatures. This frustration is expected to be in the form of blocking, and its verification is given below in $M(T)$-data obtained at high temperatures. Furthermore, as observed in the figures, the ZFC curves do not begin at $M = 0$ because, the state of the system is not in an ideal random magnetic state at room temperature, from which the sample is initially cooled down to 5 K.

To provide further support for the presence of blocking, we have measured $M(T)$ in 50 Oe of $CuFe_2O_4$/25% CuO up to 750 K using various measurement protocols. The results were shown in Fig. 8.

After the measurement in the range $10 \leq T \leq 380$ K (blue data, Fig. 8), the sample was placed in a furnace-attachment and the measurement was carried out in increasing

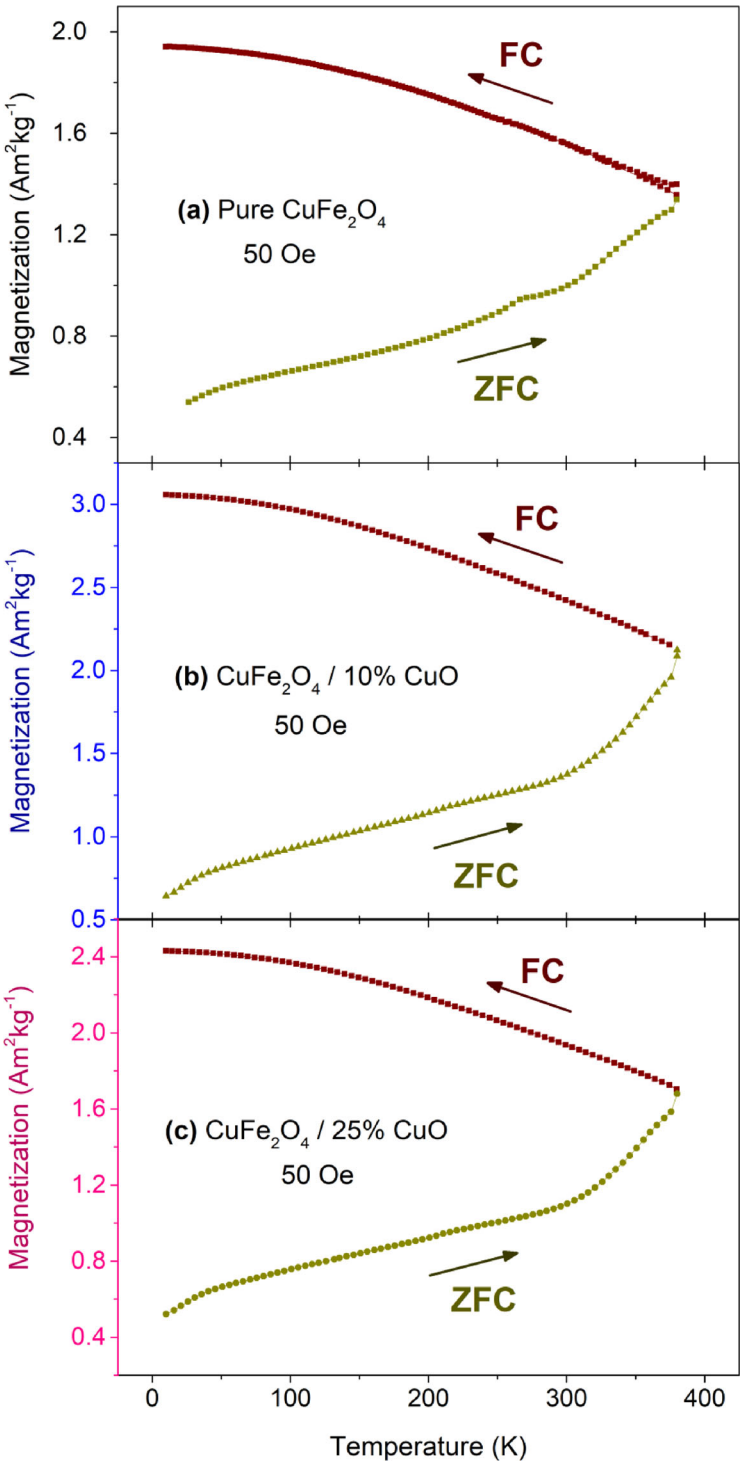

Figure 7. Magnetization versus temperature curves under ZFC and FC (50 Oe) conditions for (a) $CuFe_2O_4$, (b) $CuFe_2O_4$/10% CuO, and (c) $CuFe_2O_4$/25% CuO.

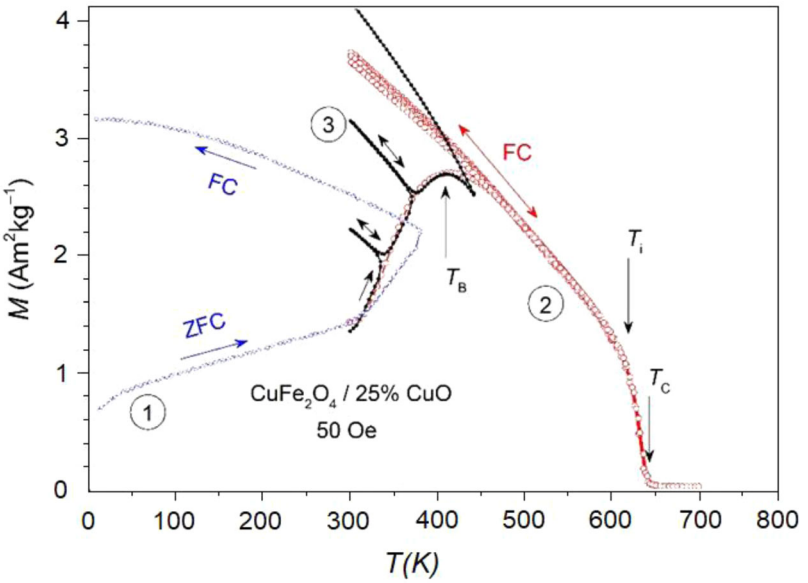

Figure 8. $M(T)$ measured with three different protocols. (1) ZFC from room temperature – FC; (2) 300 ↔ 500, 300 ↔ 550, 300 ↔ 600, 300 ↔ 650, 300 ↔ 700K; (3) 300 → 440 → 300K with intermediate cooling and rewarming steps.

and decreasing temperature directions with the sequence 300 ↔ 350, 300 ↔ 400, 300 ↔ 500, 300 ↔ 600, 300 ↔ 650, 300 ↔ 700 K (black and red data). Starting at 300 K $M(T)$ initially increases with increasing temperature and reaches a turning point identified as the blocking temperature T_B, after which it decreases with decreasing temperature and shows two further features indicated by the vertical arrows. The first is identified as the Curie temperature $T_C = 640$ K, below which the oxide orders ferrimagnetically and the second as an intermediate ordering temperature $T_i = 600$ K, where the ordering undergoes a possible reorientation of the spins. Once the sample is brought above T_B, $M(T)$ becomes retraceable between 300 and 700 K. The sample was then cooled from 700 K to 300 K in zero-field and $M(T)$ was measured on increasing temperature by pausing in steps. At each step, the temperature was first decreased and then increased again. This is shown with the double-headed black arrows. Each time the temperature is reduced, $M(T)$ remembers the temperature from where it was reduced and then it continues to increase with increasing temperature up to T_B. Such data are typical of magnetic frustration effects, which in this case can be identified as blocking. The three sets of data do not coincide exactly because of the different initial conditions of the magnetization measurements. These results confirm that the splitting in the $M(T)$ curves in Fig. 7 are caused by the blocked state of the sample. Blocking can only occur if the grain size becomes equal or less than the magnetic domain size, confirming that nano-sized grains are present in the sample.

The magnetization versus applied magnetic field $M(H)$ is also shown in Fig. 9. The hysteresis loop of pure $CuFe_2O_4$ shows nearly zero coercivity and the saturation magnetization is 22 Am^2kg^{-1} (Fig. 9(a)). On the other hand, $M(B)$ of pure CuO at room temperature shows the expected paramagnetic response as shown in Fig. 9(b).

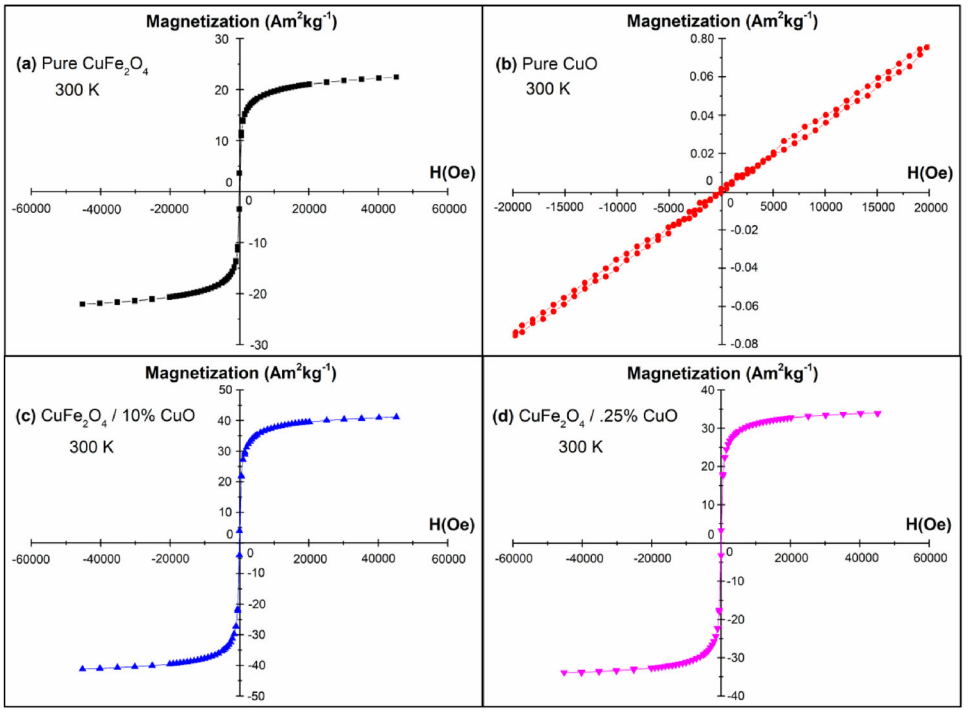

Figure 9. Magnetization versus applied magnetic field at 300 K for (a) $CuFe_2O_4$, (b) CuO, (c) $CuFe_2O_4$/10% CuO, and (d) $CuFe_2O_4$/25% CuO.

$M(B)$ of the composite samples shows a nearly vanishing coercivity. This behavior further supports the fact that these composites are superparamagnetic. The saturation magnetizations (M_S) are 40 $Am^2\ kg^{-1}$ and 33 $Am^2\ kg^{-1}$ for $CuFe_2O_4$/10% CuO and $CuFe_2O_4$/25% CuO, respectively (Fig. 9(c–d)). The reason for the lower value of M_S for $CuFe_2O_4$/25% CuO is because it contains fewer magnetic ions.

4. Conclusions

In the present study, $CuFe_2O_4$/CuO nanocomposites were synthesized by chemical co-precipitation and sol-gel methods. XRD results showed that $CuFe_2O_4$ has a cubic crystal structure. The semiconducting CuO addition to the nano-sized $CuFe_2O_4$ ferrite with different concentrations improved the dielectric and AC conductivity properties of $CuFe_2O_4$. The results of AC impedance and complex dielectric studies have been discussed in terms of Koop's model. The results of Nyquist analyses suggest a layered structure for the copper ferrite samples. In light of the investigation of AC electrical parameters, it was suggested that the $CuFe_2O_4$/25% CuO nanocomposite may be used for high-frequency applications. The temperature dependence of the magnetization showed frustration effects in copper ferrite and copper ferrite/copper oxide nanocomposites. The effect is related to the superparamagnetic property of the ferrite-based composites due to the magnetic domain size being similar to the nanometer grain size of the materials.

Funding

This research was supported by the Yildiz Technical University Scientific Research Projects Coordination Department within Project FBA-2017-3162.

ORCID

Mehmet Kılıç http://orcid.org/0000-0003-1882-0405
Naime Didem Kahya http://orcid.org/0000-0001-9255-0867
Banu Süngü Mısırlıoğlu http://orcid.org/0000-0002-9540-5718
Öznur Çakır http://orcid.org/0000-0002-0826-7880
Zeynep Güven Özdemir http://orcid.org/0000-0001-5085-5814

References

[1] K. K. Kefeni, T. A. Msagati, and B. B. Mamba, Ferrite nanoparticles: synthesis, characterisation and applications in electronic device, *Mat. Sci. Eng. B* **215**, 37 (2017). DOI: 10.1016/j.mseb.2016.11.002.

[2] M. Rashad *et al.*, Magnetic and catalytic properties of cubic copper ferrite nanopowders synthesized from secondary resources, *Adv. Powder Technol.* **23** (3), 315 (2012). DOI: 10.1016/j.apt.2011.04.005.

[3] K. Ali *et al.*, Synthesis of $CuFe_2O_4$-ZnO nanocomposites with enhanced electromagnetic wave absorption properties, *J. Alloy Compd.* **705**, 559 (2017). DOI: 10.1016/j.jallcom.2017.01.264.

[4] Z. Sun *et al.*, Simple synthesis of $CuFe_2O_4$ nanoparticles as gas-sensing materials, *Sensor Actuat. B-Chem.* **125** (1), 144 (2007). DOI: 10.1016/j.snb.2007.01.050.

[5] S. Anandan *et al.*, Magnetic and catalytic properties of inverse spinel $CuFe_2O_4$ nanoparticles, *J. Magn. Magn. Mater.* **432**, 437 (2017). DOI: 10.1016/j.jmmm.2017.02.026.

[6] R. K. Selvan *et al.*, Synthesis and characterization of $CuFe_2O_4/CeO_2$ nanocomposites, *Mater. Chem. Phys.* **112** (2), 373 (2008). DOI: 10.1016/j.matchemphys.2008.05.094.

[7] C. Murugesan *et al.*, Influence of Zn concentration on the structural and magnetic properties of nanocrystalline $Cu_{1-x}Zn_xFe_2O_4$ mixed ferrites synthesized using novel combustion method, *J. Magn. Magn. Mater.* **443**, 334 (2017). DOI: 10.1016/j.jmmm.2017.07.061.

[8] K. Verma, A. Kumar, and D. Varshney, Effect of Zn and Mg doping on structural, dielectric and magnetic properties of tetragonal $CuFe_2O_4$, *Curr. Appl. Phys.* **13** (3), 467 (2013). DOI: 10.1016/j.cap.2012.09.015.

[9] K. Ali *et al.*, Structural, dielectric and magnetic properties of SnO_2-$CuFe_2O_4$ nanocomposites, *J. Magn. Magn. Mater.* **428**, 417 (2017). DOI: 10.1016/j.jmmm.2016.11.115.

[10] C. Karunakaran *et al.*, Nanostructures and optical, electrical, magnetic, and photocatalytic properties of hydrothermally and sonochemically prepared $CuFe_2O_4/SnO_2$, *RSC Adv.* **3** (37), 16728 (2013). DOI: 10.1039/c3ra41872c.

[11] V. Manikandan *et al.*, Effect of sintering temperature on structural and dielectric properties of Sn substituted $CuFe_2O_4$ Nanoparticles, *J. Magn. Magn. Mater.* **423**, 250 (2017). DOI: 10.1016/j.jmmm.2016.09.077.

[12] R. K. Selvan *et al.*, Optimization of sintering on the structural, electrical and dielectric properties of SnO_2 coated $CuFe_2O_4$ nanoparticles, *Mater. Chem. Phys.* **99** (1), 109 (2006). DOI: 10.1016/j.matchemphys.2005.10.006.

[13] R. K. Selvan *et al.*, Effect of SnO_2 coating on the magnetic properties of nanocrystalline $CuFe_2O_4$, *Solid State Commun.* **137** (9), 512 (2006). DOI: 10.1016/j.ssc.2005.12.018.

[14] K. Ali *et al.*, Enhancement of microwaves absorption properties of $CuFe_2O_4$ magnetic nanoparticles embedded in MgO matrix, *J. Alloy Compd.* **696**, 711 (2017). DOI: 10.1016/j.jallcom.2016.10.220.

[15] K. Ali *et al.*, Synthesis, structural, dielectric and magnetic properties of $CuFe_2O_4/MnO_2$ nanocomposites, *J. Magn. Magn. Mater.* **434**, 30 (2017). DOI: 10.1016/j.jmmm.2016.12.009.

[16] V. Manikandan *et al.*, Influence of sintering temperature on structural, dielectric and magnetic properties of Li substituted $CuFe_2O_4$ nanoparticles, *J. Magn. Magn. Mater.* **426**, 11 (2017). DOI: 10.1016/j.jmmm.2016.11.034.

[17] R. K. Selvan *et al.*, $CuFe_2O_4/SnO_2$ nanocomposites as anodes for Li-ion batteries, *J. Power Sources* **157** (1), 522 (2006). DOI: 10.1016/j.jpowsour.2005.07.030.

[18] S. Kameoka, T. Tanabe, and A. P. Tsai, Self-assembled porous nano-composite with high catalytic performance by reduction of tetragonal spinel $CuFe_2O_4$, *Appl. Catal. A-Gen.* **375** (1), 163 (2010). DOI: 10.1016/j.apcata.2009.12.035.

[19] N. Nasrallah *et al.*, Photocatalytic reduction of Cr(VI) on the novel hetero-system $CuFe_2O_4$/CdS, *J. Hazard. Mater.* **185** (2–3), 1398 (2011). DOI: 10.1016/j.jhazmat.2010.10.061.

[20] S.-C. Yang *et al.*, Preparation of nano-sized Cu from a rod-like $CuFe_2O_4$: suitable for high performance catalytic applications, *Appl. Catal. B-Environ.* **106** (3–4), 650 (2011). DOI: 10.1016/j.apcatb.2011.06.030.

[21] M. A. Haija *et al.*, Characterization of H_2S gas sensor based on $CuFe_2O_4$ nanoparticles, *J. Alloy Compd.* **690**, 461 (2017). DOI: 10.1016/j.jallcom.2016.08.174.

[22] M. A. Haija *et al.*, Selective hydrogen gas sensor using $CuFe_2O_4$ nanoparticle based thin film, *Appl. Surf. Sci.* **369**, 443 (2016). DOI: 10.1016/j.apsusc.2016.02.103.

[23] S. N. Hosseini *et al.*, Oxidation and electrical behavior of $CuFe_2O_4$ spinel coated Crofer 22 APU stainless steel for SOFC interconnect application, *Solid State Ion.* **289**, 95 (2016). DOI: 10.1016/j.ssi.2016.02.015.

[24] R. Khan *et al.*, Facile synthesis of $CuFe_2O_4$–Fe_2O_3 composite for high-performance supercapacitor electrode applications, *Mater. Res. Express* **4** (10), 105501 (2017). DOI: 10.1088/2053-1591/aa8dc4.

[25] J. Pal *et al.*, Hierarchical Au–CuO nanocomposite from redox transformation reaction for surface enhanced Raman scattering and clock reaction, *CrystEngComm* **16** (5), 883 (2014). DOI: 10.1039/C3CE41766B.

[26] S. Rehman, A. Mumtaz, and S. Hasanain, Size effects on the magnetic and optical properties of CuO nanoparticles, *J. Nanopart. Res.* **13** (6), 2497 (2011). DOI: 10.1007/s11051-010-0143-8.

[27] X. Wang *et al.*, Synthesis of CuO nanostructures and their application for nonenzymatic glucose sensing, *Sensor Actuat. B-Chem.* **144** (1), 220 (2010). DOI: 10.1016/j.snb.2009.09.067.

[28] L.-B. Luo *et al.*, One-dimensional CuO nanowire: synthesis, electrical, and optoelectronic devices application, *Nanoscale Res. Lett.* **9** (1), 637 (2014). DOI: 10.1186/1556-276X-9-637.

[29] K. Ramachandran *et al.*, One pot polyol synthesis of CuO-$CuFe_2O_4$ nanocomposites and their structural, optical and electrical property studies, *Mater. Lett.* **175**, 106 (2016). DOI: 10.1016/j.matlet.2016.03.134.

[30] A. Chapelle *et al.*, Improved semiconducting $CuO/CuFe_2O_4$ nanostructured thin films for CO_2 gas sensing, *Sensor Actuat. B-Chem.* **204**, 407 (2014). DOI: 10.1016/j.snb.2014.07.088.

[31] P. Liu *et al.*, Novel heterogeneous hybrid of yolk–shell CuO@ $CuFe_2O_4$: facile synthesis and enhanced lithium-storage performance, *ChemElectroChem* **4** (8), 2068 (2017). DOI: 10.1002/celc.201700313.

[32] J. M. Kshirsagar, R. Shrivastava, and P. S. Adwani, Preparation and characterization of copper oxide nanoparticles and determination of enhancement in critical heat flux, *Therm. Sci.* **21** (1 Part A), 233 (2017). DOI: 10.2298/TSCI140619026K.

[33] V. Petříček, M. Dušek, and L. Palatinus, Crystallographic computing system JANA2006: general features, *Z. Krist-Cryst. Mater.* **229** (5), 345 (2014).

[34] C. Koops, On the dispersion of resistivity and dielectric constant of some semiconductors at audiofrequencies, *Phys. Rev.* **83** (1), 121 (1951). DOI: 10.1103/PhysRev.83.121.

[35] J. C. Maxwell, *A Treatise on Electricity and Magnetism* (Clarendon Press, Oxford, 1873).

[36] K. W. Wagner, Erklärung der dielektrischen nachwirkungsvorgänge auf grund maxwellscher vorstellungen, *Arch. Elektrotechn.* **2** (9), 371 (1914). DOI: 10.1007/BF01657322.
[37] M. B. Hossen, and A. A. Hossain, AC resistivity and frequency dependence of the dielectric properties for Al doped NiCuZn ferrites, presented at the 2012 IEEE International Conference on Informatics, Electronics & Vision (ICIEV), Dhaka, Bangladesh, 18–19 May 2012, pp. 903–907.
[38] I. Sadiq *et al.*, Structural and dielectric properties of doped ferrite nanomaterials suitable for microwave and biomedical applications, *Prog. Nat. Sci.-Mater.* **25** (5), 419 (2015). DOI: 10.1016/j.pnsc.2015.09.011.
[39] A. Lakshman *et al.*, Electrical properties of In^{3+} and Cr^{3+} substituted magnesium–manganese ferrites, *J. Phys. D: Appl. Phys.* **38** (5), 673 (2005). DOI: 10.1088/0022-3727/38/5/002.
[40] R. Kotnala *et al.*, Investigation of structural, dielectric, and magnetic properties of hard and soft mixed ferrite composites, *J. Appl. Phys.* **112** (5), 054323 (2012). DOI: 10.1063/1.4752030.
[41] C. K. Patel *et al.*, Structural phases, magnetic properties and Maxwell–Wagner type relaxation of $CoFe_2O_4/Sr_2Co_2Fe_{12}O_{22}$ ferrite composites, *Mater. Res. Express* **4** (7), 076105 (2017). DOI: 10.1088/2053-1591/aa7699.
[42] A. K. Jonscher, Dielectric relaxation in solids, *J. Phys. D: Appl. Phys.* **32** (14), R57 (1999). DOI: 10.1088/0022-3727/32/14/201.
[43] A. Oueslati *et al.*, AC conductivity analysis and dielectric relaxation behavior of $[N(C_3H_7)_4]_2Cu_2C_{l6}$, *J. Alloy Compd.* **492** (1–2), 508 (2010). DOI: 10.1016/j.jallcom.2009.11.152.
[44] H. Mahamoud *et al.*, Impedance and modulus analysis of the $(Na_{0.6}Ag_{0.4})_2PbP_2O_7$ compound, *J. Alloy Compd.* **509** (20), 6083 (2011). DOI: 10.1016/j.jallcom.2011.03.027.
[45] Z. G. Özdemir *et al.*, Super-capacitive behavior of carbon nano tube doped 11-(4-cyanobiphenyl-4-oxy) undecan-1-ol, *J. Mol. Liq.* **211**, 442 (2015). DOI: 10.1016/j.molliq.2015.07.026.